

1 **Title:** Variation of Jupiter's Aurora Observed by Hisaki/EXCEED: 1. Observed Characteristics of the  
2 Auroral Electron Energies Compared with observations performed using HST/STIS

3 **Paper:** JGR space physics

4 **Authors:** Chihiro Tao [1, 2, 3], Tomoki Kimura [4, 5], Sarah V. Badman [6], Go Murakami [4], Kazuo  
5 Yoshioka [4, 7], Fuminori Tsuchiya [3], Nicolas André [1], Ichiro Yoshikawa [7], Atsushi Yamazaki  
6 [4], Daikou Shiota [8], Hiroyasu Tadokoro [9, 10], Masaki Fujimoto [4]

7 **Affiliations:**

8 [1] IRAP, Université de Toulouse/UPS-OMP/CNRS, avenue du Colonel Roche, 31028, Toulouse,  
9 France

10 [2] now at NICT, Koganei, Japan

11 [3] Tohoku University, Miyagi, Japan

12 [4] ISAS/JAXA, Sagamihara, Japan

13 [5] now at Riken, Saitama, Japan

14 [6] Lancaster University, Lancaster, UK

15 [7] University of Tokyo, Tokyo, Japan

16 [8] STEL, Nagoya University, Nagoya, Japan

17 [9] Tokyo University of Technology, Tokyo, Japan

18 [10] now at Musashino University, Tokyo, Japan

19

20 **Corresponding Author:** Chihiro Tao (chihiro.tao@nict.go.jp)

21 **Running title** (<=45 characters): Jupiter's aurora observed by Hisaki (35)

22 (<7300)/ 500 + 6 + 1 = 15 + 7 = 22

23 **Key points** (<=100 characters):

24 1. Temporal variations of Jupiter's northern aurora were detected using Hisaki/EXCEED (82)

25 2. Auroral power enhancement are accompanied by a slight far-ultraviolet colour ratio (CR) increase  
26 (96)

27 3. CR-brightness distribution and longitude dependence are consistent with other observations (90)

28 -----

29 **Abstract** (<250 words)

30 [1] Temporal variation of Jupiter's northern aurora is detected using the Extreme Ultraviolet  
31 Spectroscopy for Exospheric Dynamics (EXCEED) onboard JAXA's Earth-orbiting planetary space  
32 telescope Hisaki. The wavelength coverage of EXCEED includes the H<sub>2</sub> Lyman and Werner bands at  
33 80–148 nm from the entire northern polar region. The prominent periodic modulation of the observed  
34 emission corresponds to the rotation of Jupiter's main auroral oval through the aperture, with additional  
35 superposed -50%–100% temporal variations. The hydrocarbon colour ratio (CR) adopted for the  
36 wavelength range of EXCEED is defined as the ratio of the emission intensity in the long wavelength  
37 range of 138.5–144.8 nm to that in the short wavelength range of 126.3–130 nm. This CR varies with  
38 the planetary rotation phase. Short- (within one planetary rotation) and long-term (> one planetary  
39 rotation) enhancements of the auroral power are observed in both wavelength ranges and result in a  
40 small CR variation. The occurrence timing of the auroral power enhancement does not clearly depend  
41 on the central meridional longitude. Despite the limitations of the wavelength coverage and the large

42 field of view of the observation, the auroral spectra and CR-brightness distribution measured using  
43 EXCEED are consistent with other observations. (198 words)

#### 44 **1. Introduction**

45 [2] Aurorae represent the environment and dynamics of a coupled magnetosphere-ionosphere -  
46 thermosphere system. Jupiter's auroral emission is often categorized into three regions: low-latitude  
47 moon-footprint emission, main aurora emission, and high-latitude polar emission (see the reviews of  
48 Clarke et al. [2004], Badman et al. [2014], Grodent [2014], and references therein). The moon-footprint  
49 aurorae are caused by the relative motion of electrically conductive moons and plasma carried by the  
50 surrounding planetary magnetic field. The main aurora emission is associated with the plasma  
51 corotation-enforcement current during the transport of the angular momentum from the planetary  
52 neutral atmosphere through the ionosphere to the magnetosphere [e.g., Hill, 2001; Cowley and Bunce,  
53 2001; Cowley et al., 2007]. Jupiter's polar region, enclosed by the main aurora, corresponds to both  
54 open and closed magnetic field lines [e.g., Vogt et al., 2011]. Several auroral features in the polar  
55 region have been related to magnetospheric reconnection events [e.g., Grodent et al., 2004], emissions  
56 at the open-closed field line boundary [Pallier and Prangé, 2004], and short-term bursts at the dayside  
57 cusp [e.g., Waite et al., 2001].

58 [3] The ultraviolet (UV) emissions of Jupiter's aurora are radiated from atmospheric molecular ( $H_2$ )  
59 and atomic hydrogen (H) excited by precipitating electrons. Jupiter's UV emission spectra show  
60 significant absorption by hydrocarbons [e.g., Yung et al., 1982]. This absorption effect is measured as  
61 the colour ratio (CR), which is defined as the ratio of the intensity of the wavelength bands unabsorbed  
62 by hydrocarbons to that of the absorbed wavelength bands. The CR represents the column density of  
63 hydrocarbons above auroral emissions because the hydrocarbons are located in the deep atmosphere.  
64 Assuming it to be related to the penetration depth of auroral electrons, the CR is used to estimate the  
65 electron energy, while the altitude profile of the hydrocarbons also modifies the CR [e.g., Livengood  
66 and Moos, 1990; Livengood et al., 1993; Gérard et al., 2003]. The auroral spectra observed using the  
67 Hubble Space Telescope (HST) Space Telescope Imaging Spectrograph (STIS) revealed that the CR  
68 varies between spatial structures [Gustin et al., 2002, 2004; Gérard et al., 2014] and shows short-term  
69 variations over a few 10s seconds [Gérard et al., 2003]. The high-latitude emissions sometimes show  
70 electron energies and energy fluxes similar to those of the main oval emissions; however, high electron  
71 energies (large CR) with low fluxes are also present [Gustin et al., 2004]. The CR related to the  
72 brightness of H Lyman- $\alpha$  and  $H_2$  has also been applied [e.g., Harris et al., 1996], which is suggested  
73 to be sensitive to lower-energy electrons because the CR refers to hydrogen atoms at a higher altitude  
74 [Tao et al., 2014].

75 [4] Continuous observations reveal several time scales of auroral variations. The auroral area visible  
76 to an observer needs to be accounted for when considering variations of the integrated auroral intensity  
77 [e.g., Prangé et al., 2001; Pryor et al., 2005] and far-UV (FUV) CR [Livengood and Moos, 1990].  
78 Prangé et al. [2001] reported a dominant intensity variation over 5–10 days associated with  
79 magnetospheric fluctuations in addition to small variations over a few hours and a longer (> six weeks)  
80 trend. A sporadic large intensity enhancement during one planetary rotation was detected by Cassini  
81 [Pryor et al., 2005]. Auroral monitoring using the HST reveals some auroral intensity enhancements  
82 when a solar wind compression region foreshock was estimated to arrive at Jupiter, while no clear  
83 correlations with reverse shocks occurred [Clarke et al., 2009]. Different auroral responses to solar  
84 wind variations were observed in sets of HST observations separated by several months [Nichols et

85 al., 2009]. The time scale of the auroral intensity variation in the polar region is as short as a few tens  
 86 of seconds, which is considered to reflect the localized solar wind variation. The short-term auroral  
 87 bursts at the dayside cusp are found when the solar wind dynamic pressure is enhanced [Waite et al.,  
 88 2001]. The periodic intensity variation with a timescale of 2–3 min is suggested to be related to the  
 89 pulsed magnetic reconnections at the dayside by analogy with similar phenomena observed on Earth  
 90 [Bonfond et al., 2011].

91 [5] Temporal variations and occurrence properties under various outer (i.e., solar wind) and inner (e.g.,  
 92 Io volcanic activity) conditions are crucial for understanding these auroral phenomena and related  
 93 magnetospheric dynamics. Our new tool for monitoring the Jovian aurora is the Extreme Ultraviolet  
 94 Spectroscope for Exospheric Dynamics (EXCEED) [Yoshioka et al., 2013; Yoshikawa et al., 2014;  
 95 Yamazaki et al., 2014] on board Japan Aerospace eXploration Agency’s (JAXA’s) Earth-orbiting  
 96 planetary telescope Hisaki. EXCEED observed extreme UV (EUV) emission from Jupiter’s northern  
 97 polar region, which was our main interest here, and the Io plasma torus continuously over 40 min of  
 98 every 106 min of the Hisaki orbit from December 2013 to April 2014. In addition, the HST  
 99 observations were also carried out during the first half of January 2014. EXCEED could detect sporadic,  
 100 large auroral intensity enhancement lasting less than one planetary rotation, which was associated with  
 101 auroral low latitude intensifications observed in the HST images [Kimura et al., 2015]. In this study,  
 102 we investigate the time variation of the CR with auroral brightness variations using the EXCEED.  
 103 Because the CR-energy relationship is model-dependent, this study refers to the CR instead of  
 104 converting it to electron energy. The parameters obtained in this study are estimated using the auroral  
 105 emission from the entire northern polar region. Spatially-resolved spectra measured through the STIS  
 106 on board the HST are referred to to check the spatial variations, as described in Section 2. EXCEED  
 107 covers different spectral ranges compared to STIS, such that we define a new CR for the EXCEED  
 108 spectral analysis. The observation details of EXCEED and analysed results, including the relationship  
 109 to modelled solar wind conditions, are described in Section 3. Section 4 concludes this paper.

## 110 **2. Spatial Variation of Aurora Detected Using HST/STIS**

111 [6] Following the HST spectral analysis by Gustin et al. [2004], we check the CR-brightness relation  
 112 using the spectra measured by HST/STIS over the first two weeks of January 2014.

### 113 **2.1 Imaging and Spectral Observations**

114 [7] In the HST observations program (ID: GO13035), the FUV-MAMA detector of the STIS obtained  
 115 FUV images and spectra of Jupiter’s northern aurora. The auroral images were obtained using a SrF<sub>2</sub>  
 116 long-pass filter to detect H<sub>2</sub> emission in the wavelength range of 125–170 nm with a plate scale of  
 117  $\sim 0.0224$  arcsec pixel<sup>-1</sup>. We used geometric distortion corrected imaging data in ‘x2d’ files with a unit  
 118 of counts s<sup>-1</sup>. The long slit with a size of  $52 \times 0.5$  arcsec<sup>2</sup> with G140L grating provides spatially  
 119 resolved spectra at wavelengths of 110–170 nm with a resolution of  $\sim 1.2$  nm. We used the flux and  
 120 wavelength calibrated two-dimensional spectra in ‘x2d’ files with a unit of erg s<sup>-1</sup> cm<sup>-2</sup> Å<sup>-1</sup> arcsec<sup>-2</sup>.  
 121 On each HST orbit, the observations were made in the following sequence, image (700 s), spectrum  
 122 (200 s), and image (736 s), using a time-tag mode, such that the exposure time could be divided into  
 123 shorter integration times. We use the time-integrated spectra and images over each interval in this  
 124 analysis. This sequence was repeated for 14 HST orbits spaced over two weeks. The intensity profiles  
 125 from the filtered images were compared to the slit spectra across the full wavelength range by  
 126 accounting for the filter throughput the function. The slit position in the north-south direction is

127 determined by the position of the limb, and that in the east-west direction was determined by matching  
 128 the intensity profile along the slit with the profiles from the images obtained before and after the  
 129 spectral observations. The date, time, and System III central meridional longitude (CML) of the  
 130 spectral and image observations used in this study are summarized in Table 1.

## 131 2.2 Results

132 [8] Figure 1a shows the HST image and slit position of the spectral observation (white vertical line)  
 133 obtained on the same HST orbit on 2 January 2014. The slit crosses from the top to the bottom, the  
 134 main auroral oval at the limb, faintly enhanced high-latitude emission, and the main auroral oval on  
 135 the disk. These three regions are seen in the spatial profile of the auroral brightness along the slit (left  
 136 of Figure 1b), as shown by light blue, red, and blue lines, respectively. Figures 1c and 1d show the  
 137 image and profile obtained on 7 January in the same format. The emission intensity of the main aurora  
 138 on 7 January was lower except for localized enhancement around noon at the limb. The high-latitude  
 139 emission is faint in the region under the slit (Figure 1d). The localized bright high-latitude emission is  
 140 detected in the auroral image (Figure 1c). The typical FUV CR used for the STIS spectra is defined as  
 141 the intensity ratio between the wavelength bands unabsorbed by the hydrocarbons  $I_{(155-162\text{ nm})}$  and the  
 142 wavelength bands absorbed by the hydrocarbons  $I_{(123-130\text{ nm})}$ , i.e.

$$143 \quad \text{CR}_{\text{STIS}} = I_{(155-162\text{ nm})} / I_{(123-130\text{ nm})} \quad , \quad (1)$$

144 where  $I$  is the height-integrated intensity of the emission, e.g., in units of kilo-Rayleigh (kR) or photons  
 145  $\text{s}^{-1}$  integrated over the wavelength of the subscript. The absorption cross section of methane is shown  
 146 using the blue line in Figure 2c. The STIS spectra are provided in energy flux units, while the CR is  
 147 provided in photon flux units. A ratio of (155–162 nm)/(123–130 nm) obtained from the original STIS  
 148 spectra is multiplied by 1.25 to account for the unit change. For simplicity, the viewing angle is not  
 149 considered in our procedure, i.e.,  $\text{CR}_{\text{STIS}}$  is derived using the emission in each pixel. The  $\text{CR}_{\text{STIS}}$  values  
 150 2 and 8 are related to electron mean energies of 60 keV and 170 keV, respectively, for an eddy diffusion  
 151 coefficient of  $1.4 \times 10^6 \text{ cm}^2 \text{ s}^{-1}$  at the homopause (see Gérard et al. [2003] for details). The  $\text{CR}_{\text{STIS}}$   
 152 profiles along the slit (right of Figures 1b and 1d) vary up to  $\sim 6$ , with larger values in the high-latitude  
 153 region and the main oval on the disk. The time variations of the emitted power at these wavelengths  
 154 and  $\text{CR}_{\text{STIS}}$  for the entire HST campaign are shown in Figure 1e and Table 1. The intensities are  
 155 integrated over 200 s. The signal-to-noise ratio is high as indicated by the short error bars. The  
 156 relationship between the unabsorbed brightness at wavelengths of 155–162 nm and  $\text{CR}_{\text{STIS}}$  varies  
 157 between the spatial regions (Figure 1f).  $\text{CR}_{\text{STIS}}$  increases with the emitted power at the main auroral  
 158 oval (light blue pluses and blue crosses).  $\text{CR}_{\text{STIS}}$  in the high-latitude region (red diamonds) has two  
 159 components: one component is similar to the main aurora, and the other component shows a lower  
 160 intensity and higher  $\text{CR}_{\text{STIS}}$ .

161 [9] This relationship is comparable with the relationship between the electron energy and electron  
 162 energy flux derived by Gustin et al. [2004]. Their main auroral oval and high-latitude regions  
 163 correspond to the main aurora at the disk and high-latitude emission here, respectively. The regional  
 164  $\text{CR}_{\text{STIS}}$ -brightness relation obtained here is consistent with their results from a different dataset. The  
 165  $\text{CR}_{\text{STIS}}$  at the limb takes small values, as also observed by Gustin et al. [2002] and Gérard et al. [2014].

## 166 3. Temporal Variation of the Aurora Detected Using Hisaki/EXCEED

### 167 3.1 Observations

168 [10] EXCEED counts EUV photons as a function of the position along the slit and wavelength  
 169 dispersion. We used the dataset obtained using the dumbbell-shaped slit, which detected emissions  
 170 from the Io plasma torus and Jupiter's northern polar region simultaneously. The slit shapes and a  
 171 sample imaging spectrum are shown in Figures 2a and 2b, respectively. The slit width in the polar  
 172 region is 20 arcsec in the north-south direction (along Jupiter's rotation axis) with an effective spatial  
 173 resolution along the slit (dawn-dusk direction) of 17 arcsec [Yoshikawa et al., 2014] and a pointing  
 174 accuracy of  $\pm 2$  arcsec. The red solid lines in Figure 1a show the coverage of the EXCEED auroral  
 175 aperture in the northern hemisphere. The dataset excluded times when Jupiter was eclipsed by the  
 176 Earth or Hisaki was located in the southern atlantic anomaly. Under the latter, the instruments were  
 177 turned off to avoid effects of energetic particles precipitated from the terrestrial radiation belts. Here,  
 178 we analyse the data obtained from 21 December 2013 to 31 January 2014 when the EXCEED time  
 179 coverage was maximum. EXCEED detects auroral emission in the wavelength range of 80–148 nm,  
 180 covering part of the H<sub>2</sub> Lyman (B  $\rightarrow$  X) and Werner (C  $\rightarrow$  X) band emissions with a full width at half  
 181 maximum resolution of 0.3 nm. We convert the photon counts arriving at the EXCEED detector into  
 182 the photon flux at each wavelength referring to the effective area [Yoshikawa et al., 2014]. Then, the  
 183 number flux is converted into energy flux and integrated over a half hemisphere assuming isotropic  
 184 emission to derive the total emitted power. Figure 2c shows the spectra measured using STIS (black  
 185 line) and EXCEED (red line) close in time. Except for the geocoronal emission range (e.g., around  
 186 121.6 nm Lyman- $\alpha$ ) and spectral edges, the spectra observed using EXCEED and STIS are consistent.  
 187 The data are integrated over certain wavelength bands (described in Section 3.2) and over 10 min to  
 188 improve the signal-to-noise ratio, such that the variations in the northern auroral activity over time  
 189 scales from a few tens of minutes to a few months are detected. The long temporal coverage of the  
 190 average auroral activity provided by the EXCEED dataset is complementary to the short temporal  
 191 (~seconds) and spatial variations observed with STIS (e.g., Gérard et al. [2003], Gustin et al. [2004],  
 192 Gérard et al. [2014], and Section 2.2).

### 193 3.2 CR for EXCEED

194 [11] EXCEED covers a wavelength range up to 148 nm, such that the CR<sub>STIS</sub> given by Eq. (1) is not  
 195 directly applicable. An alternate CR<sub>EXCEED</sub> is defined as

$$196 \quad \text{CR}_{\text{EXCEED}} = I_{(138.5-144.8 \text{ nm})} / I_{(126.3-130 \text{ nm})}. \quad (2)$$

197 We selected these two wavelength ranges for CR<sub>EXCEED</sub> using the following criteria: (i) the CH<sub>4</sub>  
 198 absorption cross section is significantly different in the two wavelength ranges, (ii) H<sub>2</sub> self-absorption  
 199 is not effective at these wavelengths, i.e., >120 nm [e.g., Gustin et al., 2013], and (iii) EXCEED has  
 200 good sensitivity. A factor of (144.8+138.5)/(130+126.3)=1.10 is multiplied to the ratio of the  
 201 intensities in power units for EXCEED, as for CR<sub>STIS</sub> in Section 2.2.

202 [12] We used the 14 STIS spectral observations to determine the relationship between CR<sub>STIS</sub> and  
 203 CR<sub>EXCEED</sub>. For each observation, a spectrum from the main oval (blue crosses), high-latitude (red  
 204 diamonds), and limb auroral regions (light-blue pluses) was obtained and used to derive the two CRs  
 205 (Figure 2d). The expected ideal relation of CR<sub>STIS</sub> and CR<sub>EXCEED</sub> represented by the dot-dashed line is  
 206 based on the CH<sub>4</sub> absorption cross section (see Appendix for details). The derived values follow the  
 207 ideal relation in the small CR range (CR<sub>STIS</sub> <2.5, CR<sub>EXCEED</sub> <1.2) as expected; however, departures  
 208 from the ideal relation increase at larger CR. Although the absorption by methane is dominant,  
 209 acetylene (C<sub>2</sub>H<sub>2</sub>) and ethane (C<sub>2</sub>H<sub>6</sub>), which have a significant absorption cross section up to 145 nm,  
 210 should also affect our estimations of the CR. The brightness derived from the less-absorbed wavelength

211 bands selected for the STIS (155–162 nm) and EXCEED (138.5–144.8 nm) show two linear relations  
 212 (Figure 2e). The brightness from the main aurora around the limb (light-blue pluses) shows one linear  
 213 relation with a slope of approximately 0.26 (light blue dotted line), and the brightness in the other  
 214 regions (blue crosses and red diamonds) also show linearity with a shallower slope. The former would  
 215 be largely contributed by high-altitude emission, which is less affected by the hydrocarbon absorption.  
 216 For the disk emission subject to absorption, H<sub>2</sub> emission at wavelengths of 138.5–144.8 nm is  
 217 attenuated more than that at 155–162 nm by hydrocarbons. Because this attenuation decreases  
 218 CR<sub>EXCEED</sub> through its numerator, CR<sub>EXCEED</sub> increases less rapidly than CR<sub>STIS</sub>. When CR<sub>STIS</sub> increases  
 219 (>3), the absorption at 138.5–144.8 nm becomes more important because the ethane optical depth  
 220 becomes significant. We obtain the modified CR<sub>EXCEED</sub> using the brightness in the wavelength range  
 221 of 138.5–144.8 nm replaced by the expected linear relation (the dotted line in Figure 2e) referring to  
 222 the unattenuated band of CR<sub>STIS</sub>. In this modified estimation, the relation between CR<sub>STIS</sub> and the  
 223 modified CR<sub>EXCEED</sub> closely follows the expected relation (shown in Figure 2f). Because EXCEED  
 224 integrates over various regions with weak and strong hydrocarbon absorption, the application of this  
 225 conversion factor is not simple, such that we do not apply this modification in this and a companion  
 226 paper [Tao et al., accepted]. This analysis also highlights the possible discrepancy in the brightness  
 227 and CR<sub>EXCEED</sub> caused by this wavelength band selection and the observing geometry. Owing to the  
 228 monotonic relation of the CRs, the aforementioned modification does not qualitatively affect the main  
 229 results of this as well as the companion papers.

230 [13] Here, we briefly estimate the CR<sub>EXCEED</sub> variations comparable with the previous observations.  
 231 The measurements of CR<sub>STIS</sub> at the main oval vary between 1.5 and 5 and can reach ~10 [Gustin et al.,  
 232 2002, 2004]. In the CR defined by Livengood and Moos [1990],  $CR = I_{(155.7-161.9 \text{ nm})}/I_{(123-130 \text{ nm})} \times$   
 233  $(1300-1230)/(1619-1557)$ , wavelength ranges close to those used to define CR<sub>STIS</sub> are used. They  
 234 applied this result to earlier International Ultraviolet Explore (IUE) observations to find CR variations  
 235 mainly in the range of 1–5, sometimes increasing up to ~8. According to the ideal CR<sub>STIS</sub>–CR<sub>EXCEED</sub>  
 236 relation, a variation between the values of 0.7–2 with a maximum of ~5 is expected.

### 237 3.3 Spatial Integration Effect of the EXCEED Observations

238 [14] We check (1) the effect of spatial integration along the slit on the derived emitted powers and CR  
 239 using the STIS spectral dataset and (2) a hypothesis that a large CR and a small brightness derived  
 240 from the EXCEED data can also represent a relative enhancement of the high-latitude emission. We  
 241 derive the CR<sub>EXCEED</sub>-brightness relation from the auroral brightness spatially averaged over the entire  
 242 auroral region under the STIS slit, shown by the squares in Figure 3. The relation derived from the  
 243 observations performed on 2 January (event #2) are located almost centrally between the CR<sub>EXCEED</sub>-  
 244 brightness relations of different auroral components, i.e., the main aurora (blue cross), high-latitude  
 245 emission (red diamond), and main aurora at the limb (light blue plus), as shown in Figure 3a. The ratio  
 246 of the high-latitude brightness to the brightness integrated along the slit is 0.24 for this event. A similar  
 247 distribution is seen from the observation on 7 January (event #7), with a smaller high-latitude-to-total  
 248 brightness ratio of 0.14 owing to the faint high-latitude feature captured under the slit (Figure 3b).  
 249 Therefore, the CR<sub>EXCEED</sub>-brightness relations derived from the auroral brightness integrated over the  
 250 full auroral region are intermediate between the values determined for different spatial regions. This  
 251 can be representative of the EXCEED field of view over the entire northern auroral region as described  
 252 in the following sections. Figure 3c shows the spatially integrated CR<sub>EXCEED</sub>-brightness relations,  
 253 colour-coded according to the polar brightness ratio, for all cases. Relatively large polar brightness

254 events ( $>0.4$ ) are seen with small average brightness,  $(0.4-1.2)\times 10^{-13}$  mW m<sup>-2</sup> arcsec<sup>-2</sup>, and CR<sub>EXCEED</sub>  
 255  $\sim 1-1.2$ . The only exceptional event with a high brightness of  $\sim 2.4\times 10^{-12}$  mW m<sup>-2</sup> arcsec<sup>-2</sup> and CR<sub>EXCEED</sub>  
 256 of  $\sim 1$  is observed on 13 January. In addition, events with a smaller polar brightness ratio of  $\sim 0.2$  are  
 257 also seen at similar brightness-CR<sub>EXCEED</sub> values. Therefore, this dataset cannot establish the spatially  
 258 resolved analysis.

### 259 3.4 Temporal Variations of the EXCEED Observations

260 [15] Figure 4 shows the time variations of the auroral emitted power observed with EXCEED from 21  
 261 December 2013 (day of year 2014, DOY -10) to 31 January 2014 (DOY 31). The power emitted at  
 262 wavelengths of 138.5–144.8 nm (Figure 4a) and 126.3–130 nm (Figure 4b) varies over several time  
 263 scales. Over the timescale of one planetary rotation, the emitted power at 138.5–144.8 nm changes  
 264 from  $\sim 10$  to  $\sim 40$  GW. The upper limit of the observed emitted power varies more than the lower limit,  
 265 i.e.,  $\sim 20$  GW at DOY 15,  $\sim 40$  GW at DOY 0–10, and  $\sim 60$  GW at DOY  $\sim 20$  and DOY -7. In addition,  
 266 two different types of enhancement can be seen. The first type is short-term, occurring within one  
 267 planetary rotation, on DOYs 4, 11, and 14, as reported by Kimura et al. [2015] (the periods shown  
 268 using the orange horizontal lines in Figure 4a). The other type of enhancement is long-term (lasting  
 269 several planetary rotations, the periods shown using the light blue lines) at DOY -10 to -6, DOY 1–2,  
 270 and DOY 17–27. The power emitted at 126.3–130 nm also varies similarly.

271 [16] The power emitted at wavelengths of 138.5–144.8 nm has a clear CML dependence, as shown in  
 272 Figure 5a. The dashed red line shows the length of the dayside auroral oval on the visible disk as a  
 273 function of the CML. This length is obtained from the region in the northern ionosphere mapping to  
 274 an L-value of 30 using the VIP4 magnetic field model plus the ring current contribution (Table 4 of  
 275 Connerney et al. [1998]). The red solid line shows this scaled profile with a constant added to match  
 276 the magnitude of the observed emitted power profile. The average of the emitted power in 36 CML  
 277 bins is shown using the green lines. Their profile in CML is comparable with that of the scaled visible  
 278 auroral area (red solid line). The EXCEED observation includes emission from the entire region  
 279 including those inside and outside the auroral oval, which adds variations in the CML dependence.  
 280 According to the observation of Jupiter's auroral emission performed using the Cassini/UVIS at 111.5–  
 281 191.2 nm, the background disk emission can be small compared to the auroral emission in the  
 282 wavelength range covered by EXCEED below 148 nm [Pryor et al., 2005]. Airglow emission and  
 283 aurora at the limb can affect the derived emitted power in addition to the background disk emissions,  
 284 as seen by the non-zero emitted power detected at a CML of  $\sim 0^\circ$  when the aurorae are on the anti-  
 285 observer/nightside of the planet. In order to minimize these effects, the auroral emitted powers are  
 286 derived by subtracting a 5-day running average of the emitted powers measured when  $0^\circ < \text{CML} <$   
 287  $30^\circ$ . The subtracted power (7–15 GW) is smaller than the auroral dynamic variation (15–80 GW).

288 [17] The revised auroral emitted power at wavelengths of 138.5–144.8 nm is shown in Figure 4c, and  
 289 that at 126.3–130 nm is shown in Figure 4d. CR<sub>EXCEED</sub> is derived as the ratio of the background-  
 290 subtracted emitted powers, and large signal-to-noise ( $>1.5$ ) data are used. Figure 4e shows the observed  
 291 CR<sub>EXCEED</sub> during this period is in the range of 0.8–2, and sometimes enhances to  $\sim 4.5$ , which is  
 292 comparable with the previous observations described in Section 3.2. The values of CR<sub>EXCEED</sub> during  
 293 the short- or long-term auroral enhancements are similar to those before and after the events, except  
 294 for the CR<sub>EXCEED</sub> enhancement after DOY 20. Figure 4f shows the auroral emitted power at  
 295 wavelengths of 138.5–144.8 nm scaled for visibility of the auroral region by multiplying the factor  
 296 (maximum visible auroral length at all CMLs)/(visible auroral length at instantaneous CML). A short-

297 term enhancement on DOY 8 becomes visible in addition to the three other short-term events. Long-  
 298 term variations are similar to those described above with modified amplitudes.

### 299 **3.5 Solar Wind Model and Comparison with Aurora**

300 [18] We compare the auroral variation with solar wind parameters predicted using different models. A  
 301 one-dimensional (1D) magnetohydrodynamic (MHD) model propagates the observed solar wind  
 302 conditions around Earth to Jupiter [Tao et al., 2005]. For the model input, we use OMNI 1-h data,  
 303 which is a calibrated solar wind archive based on solar wind observations around the Earth (e.g.,  
 304 [http://omniweb.gsfc.nasa.gov/html/ow\\_data.html](http://omniweb.gsfc.nasa.gov/html/ow_data.html)). During the observations from 21 December 2013  
 305 to 31 January 2014 of interest here, Jupiter was located at opposition on 6 January and the Earth-Sun-  
 306 Jupiter angle was small enough ( $<30^\circ$ ) to estimate the arrival time of solar wind pressure enhancement  
 307 with a good accuracy of  $\sim 1$  day [Tao et al., 2005]. The weakness of the 1D model is the treatment of  
 308 the longitudinal variation, e.g., localized disturbance related to coronal mass ejections (CMEs), which  
 309 pass either Jupiter or Earth. We confirm that the longitudinal-limited structures are not probable during  
 310 the investigated term before mid-January referring to 3D models of ENLIL [e.g., Odstrcil and Pizzo,  
 311 1999] and SUSANOO [Shiota et al., 2014]. We also refer to a 3D model. SUSANOO solves 3D MHD  
 312 propagation of the solar wind parameters from the vicinity of the Sun based on synoptic maps of the  
 313 photospheric magnetic field provided by the Global Oscillation Network Group (GONG) and empirical  
 314 models. Good accuracy in predicting the interplanetary magnetic field (IMF) sectors using the 3D  
 315 model is evaluated at the positions of planets (see details in Shiota et al. [2014]). A difference in the  
 316 predicted arrival time of solar wind at Jupiter of  $\pm 1$  day can be brought by an ambiguity of  $\pm 20 \text{ km s}^{-1}$   
 317 if the propagation velocity is  $400 \text{ km s}^{-1}$ , while 3D MHD models also provide at least this ambiguity  
 318 so far.

319 [19] Large enhancements in dynamic pressure ( $> 0.1 \text{ nPa}$ ) lasting a few days on DOYs  $\sim -6, 1-4$ , and  
 320  $17-21$  are predicted by both the 1D and 3D SUSANOO models with less than two day difference in  
 321 the arrival time between the two models (Figure 4g). A pressure enhancement on DOYs  $12-14$  is only  
 322 predicted with the 3D model, while that on DOY  $26-28$  is only found using the 1D model. The  
 323 enhanced pressure events obtained in both models are close to the auroral brightness enhancement  
 324 lasting longer than one planetary rotation (light blue lines in Figure 4f). The short-term (less than one  
 325 planetary rotation) enhancements of the auroral brightness have a shorter duration than the solar wind  
 326 pressure variation. The auroral response to the solar wind pressure enhancement on DOY  $26-28$  is not  
 327 clear, which would be partly due to the continued auroral enhancement after DOY 17. The cross-  
 328 correlation coefficients between the auroral revised power averaged over 0.2 day and the solar wind  
 329 model show a weak correlation with maximum correlation coefficients of 0.28 for the 1D model and  
 330 0.35 for the 3D model with a one day lag, despite the ambiguity of the solar wind models. The solar  
 331 wind radial velocity is small ( $< 500 \text{ km s}^{-1}$ , Figure 4h) in both models. The CR shows a less clear  
 332 dependence on the solar wind parameters. The IMF sector is mainly ‘away’, i.e., directed outward from  
 333 the Sun, before DOY  $\sim 3$  and after DOY 12, and becomes ‘toward’ to the Sun at other times (Figure 4i).  
 334 From the 1D model, the sector is judged from the azimuthal component of the IMF. The IMF sectors  
 335 estimated using the 1D model are consistent with those obtained using the 3D model (Figure 4i).

### 336 **3.6 CML Dependence**

337 [20] The CML dependence of the auroral emission was examined in previous studies [e.g., Livengood  
 338 and Moos, 1990]. We analyse it using the EXCEED data to evaluate its stability and to find whether



339 the EXCEED parameters are consistent with it. The power emitted at wavelengths of 138.5–144.8 nm  
 340 has a clear CML dependence reflecting the fraction of the aurora visible to an observer as seen in  
 341 Section 3.3 and Figure 5a. The  $CR_{EXCEED}$  with large signal-to-ratio ( $>1.5$ ) is shown as a function of  
 342 CML in Figure 5b. Both the power and CR vary with the CML. The emitted power maximizes at CML  
 343 of  $\sim 170^\circ$ . This is a bit lower than that the CML at which the visible auroral area maximizes. The  
 344  $CR_{EXCEED}$  maximizes at a slightly higher CML of  $\sim 260^\circ$ . The average and variance  $\sigma$  of these  
 345 parameters in each CML bin are shown using the green line and its error bar, respectively. Because the  
 346 variance of the emitted power is large enough compared to its errors (grey lines in Figure 4a), the  
 347 deviation from the average behaviour is significant. On the other hand, the error is large and  
 348 comparable to the variance  $\sigma$  for the  $CR_{EXCEED}$  case for several points.

349 [21] Next, we show the temporal variation of the CML dependence of the emitted power (Figure 5c)  
 350 and  $CR_{EXCEED}$  (Figure 5d). The differences from the average values in each CML bin are shown using  
 351 the colour maps, where the white parts indicate no available data. It is difficult to find specific CML  
 352 dependences of the auroral brightness enhanced events in this dataset. For example, a short-term  
 353 enhancement occurs at CMLs of  $120^\circ$ – $180^\circ$  on DOY 11 (small enhancement by  $\sim\sigma$ ), and at CMLs of  
 354  $150^\circ$ – $250^\circ$  on DOY 14 (large enhancement by  $>2\sigma$ ). Long-term events, e.g., until DOY-5, DOY 1–2,  
 355 and DOY 17–27, show enhancements over large CML ranges. The enhancement of the flux ratio by  
 356  $>\sigma$  above the averaged profile also does not show a clear CML dependence.

357 [22] The CML offsets of the peak emitted power and CR values from the auroral visibility profile  
 358 exhibit the same trends as reported by Livengood and Moos [1990], i.e., the peak emitted power at a  
 359 lower CML and the peak CR at a higher CML. An enhancement of the CR in the dawnside region ( $\sim 8$   
 360 h magnetic local time) was reported using the spatially-resolved HST spectral analysis by Gustin et al.  
 361 [2004]. The distorted northern main auroral oval provides a better view of the dawnside at CMLs larger  
 362 than  $\sim 200^\circ$ , which might cause the shift in the CML of the peak CR.

### 363 **3.7 CR-Brightness Relations from the EXCEED Observations**

364 [23] The CR-power relations from the EXCEED observations are shown in Figure 6a. Because the  
 365 high-latitude-integrated power varies with the CML owing to the auroral aperture, we change the  
 366 power by multiplying by the factor (the maximum visible auroral length in the all CML)/(the visible  
 367 auroral length at instantaneous CMLs). The CR-power relation is modified as shown in Figure 6b. The  
 368 distribution in the auroral emitted power and  $CR_{EXCEED}$  map exhibits a triangular envelope. The lower  
 369 edge is at  $CR_{EXCEED} \sim 0.7$ – $1.5$  with the emitted power increase from  $\sim 10$  to 70 GW. The upper edge  
 370 of the envelope increases linearly with the emitted power from  $\sim 8$  to 25 GW, reaching a maximum  
 371  $CR_{EXCEED}$  of  $\sim 2.2$ . At a power greater than 25 GW, the upper edge of the envelope decreases, seeming  
 372 to approach  $CR_{EXCEED}$  of  $\sim 1.4$  for the greatest emitted power. This behaviour suggests that the large  
 373 emitted power events are mainly caused by primary particles with low average energies that are not  
 374 significantly attenuated by the hydrocarbons. A few points with lower  $CR_{EXCEED}$  values appear at the  
 375 lowest power values and others outside the triangular concentration have large uncertainties. This is  
 376 comparable with the STIS results (Figure 1f) with less scatter because of the spatial integration (Figure  
 377 3c, Section 3.3).

## 378 **4. Conclusions**

379 [24] Auroral spectra with a good time resolution ( $\sim 10$  min.) and a long coverage of over  $\sim 40$  days  
 380 obtained using Hisaki/EXCEED provide a unique opportunity to investigate the temporal variation of

381 Jupiter's auroral parameters. The brightness-CR relation obtained from the EXCEED observations is  
 382 compared with that obtained from the spatially resolved STIS observations. The main results from the  
 383 observations from the end of 2013 to January 2014 are summarized as follows.

384 [25] (1) The EXCEED results are consistent with the STIS and previous observations in their auroral  
 385 spectral profile, CML dependence, and CR-brightness distribution despite the limitation of the  
 386 different wavelength coverage and large field of view of EXCEED.

387 [26] (2) The enhancement of the auroral brightness by a factor of 2–5 over short- (< one planetary  
 388 rotation) and long-duration (> one planetary rotation) intervals are observed at both wavelength bands  
 389 that are absorbed and unabsorbed by hydrocarbons. Therefore, compared to the brightness variation,  
 390 the CR is relatively constant during this enhancement. Because the temporal variations of the solar  
 391 wind dynamic pressure are different between the 1-D and 3-D models, decisive assessments of  
 392 correlations between the aurora and solar wind parameters cannot be made. This study still suggests  
 393 that the long-term large enhancement of the auroral power could be correlated with the large solar  
 394 wind dynamic pressure enhancement. Further statistical survey is planned as future work.

395 [27] (3) The variability of the integrated auroral emitted power over the polar region is mainly  
 396 attributed to the rotation of Jupiter's main auroral oval with the planet. The auroral CR also varies with  
 397 a low dependence on the planetary rotation phase. A clear CML dependence of either short- or long-  
 398 term auroral emitted power enhancements is not apparent from the averaged CML dependence.

399 [28] The quantitative estimation of the auroral parameters (2) and further exploration of electron origin  
 400 are described in the companion paper [Tao et al., accepted]. The EXCEED observations and these  
 401 findings cover spatially integrated auroral features and therefore represent the activity of the auroral  
 402 region as a whole. Localized auroral features should exist, as shown by previous auroral observations  
 403 [e.g., Gérard et al., 2014], which will be one of the targets of upcoming Juno observations. In addition,  
 404 examination of these characteristics is also planned using the next EXCEED Jupiter observing season,  
 405 from the end of 2014 to early 2015 and beyond. Comparison with direct solar wind monitoring by Juno  
 406 during its cruising phase is also expected.

## 407 **Appendix A**

408 [29] The relation between colour ratios  $CR_{EXCEED}$  and  $CR_{STIS}$ , which are referring to different  
 409 wavelength ranges, are represented by the hydrocarbon absorption cross sections [Gustin et al., 2002].  
 410 The observed spectral intensity including absorption by dominant absorber  $CH_4$  can be expressed in  
 411 terms of absorption cross section  $\sigma$  of  $CH_4$ ,  $CH_4$  column density  $N_{CH_4}$ , and unabsorbed height-  
 412 integrated spectrum intensity  $I'$  as

$$413 \quad I_{(138.5-144.8 \text{ nm})} = I'_{(138.5-144.8 \text{ nm})} \exp(-N_{CH_4} \sigma_{(138.5-144.8 \text{ nm})}). \quad (A1)$$

414 Using this and similar relations for other wavelength ranges, we obtain the following expressions for  
 415 the CRs as

$$416 \quad CR_{STIS} = I_{(155-162 \text{ nm})} / I_{(123-130 \text{ nm})}$$

$$417 \quad = I'_{(155-162 \text{ nm})} / I'_{(123-130 \text{ nm})} \exp\{-N_{CH_4} (\sigma_{(155-162 \text{ nm})} - \sigma_{(123-130 \text{ nm})})\}, \quad (A2)$$

$$418 \quad CR_{EXCEED} = I_{(138.5-144.8 \text{ nm})} / I_{(126.3-130 \text{ nm})}$$

$$419 \quad = I'_{(138.5-144.8 \text{ nm})} / I'_{(126.3-130 \text{ nm})} \exp\{-N_{CH_4} (\sigma_{(138.5-144.8 \text{ nm})} - \sigma_{(126.3-130 \text{ nm})})\}. \quad (A3)$$

420 Substituting  $N_{\text{CH}_4}$  obtained from Eq. (A2) into Eq. (A3),

$$421 \quad \text{CR}_{\text{EXCEED}} = I'_{(138.5-144.8 \text{ nm})} / I'_{(126.3-130 \text{ nm})} \times \{\text{CR}_{\text{STIS}} I'_{(123-130 \text{ nm})} / I'_{(155-162 \text{ nm})}\}^{\beta} \quad (\text{A4})$$

$$422 \quad \beta \equiv (\sigma_{(138.5-144.8 \text{ nm})} - \sigma_{(126.3-130 \text{ nm})}) / (\sigma_{(155-162 \text{ nm})} - \sigma_{(123-130 \text{ nm})}), \quad (\text{A5})$$

423 where  $I'_{(155-162 \text{ nm})} / I'_{(123-130 \text{ nm})} = 1.1$  [e.g., Grodent et al., 2001; Gérard et al., 2014],  $I'_{(138.5-144.8 \text{ nm})} /$   
 424  $I'_{(126.3-130 \text{ nm})} = 0.59$  (estimated using the STIS spectra), and  $\sigma_{(126.3-130 \text{ nm})} = 1.73 \times 10^{-17} \text{ cm}^2$ ,  $\sigma_{(138.5-}$   
 425  $144.8 \text{ nm}) = 5.70 \times 10^{-19} \text{ cm}^2$ ,  $\sigma_{(123-130 \text{ nm})} = 1.74 \times 10^{-17} \text{ cm}^2$ , and  $\sigma_{(155-162 \text{ nm})} = 5.33 \times 10^{-24} \text{ cm}^2$  are derived  
 426 from Parkinson et al. [2006].

427

## 428 Acknowledgements

429 [30] We acknowledge the working teams of Hisaki/EXCEED, WIND, ACE, and OMNI. This work is  
 430 also based on observations made using the NASA/ESA Hubble Space Telescope (observation ID:  
 431 GO13035), obtained at the Space Telescope Science Institute (STScI), which is operated by AURA,  
 432 Inc. for NASA. HST data are available from STScI. The data of the Hisaki spacecraft are in the Data  
 433 Archives and Transmission System (DARTS) of JAXA. ENLIL simulation results were provided by  
 434 the Community Coordinated Modeling Center at the Goddard Space Flight Center through their public  
 435 runs on request system (<http://ccmc.gsfc.nasa.gov>). The CCMC is a multi-agency partnership between  
 436 NASA, AFMC, AFOSR, AFRL, AFWA, NOAA, NSF and ONR. The ENLIL model was developed  
 437 by D. Odstrcil at the University of Colorado at Boulder. The OMNI data used for the 1D solar wind  
 438 model is taken from the NASA Coordinated Data Analysis Web (CAWeb). This research was partly  
 439 supported by a grant-in-aid for scientific research from the Japan Society for the Promotion of Science  
 440 (JSPS, 15K17769). SVB was supported by the Royal Astronomical Society Research Fellowship. We  
 441 thank the referees for their productive and valuable comments.

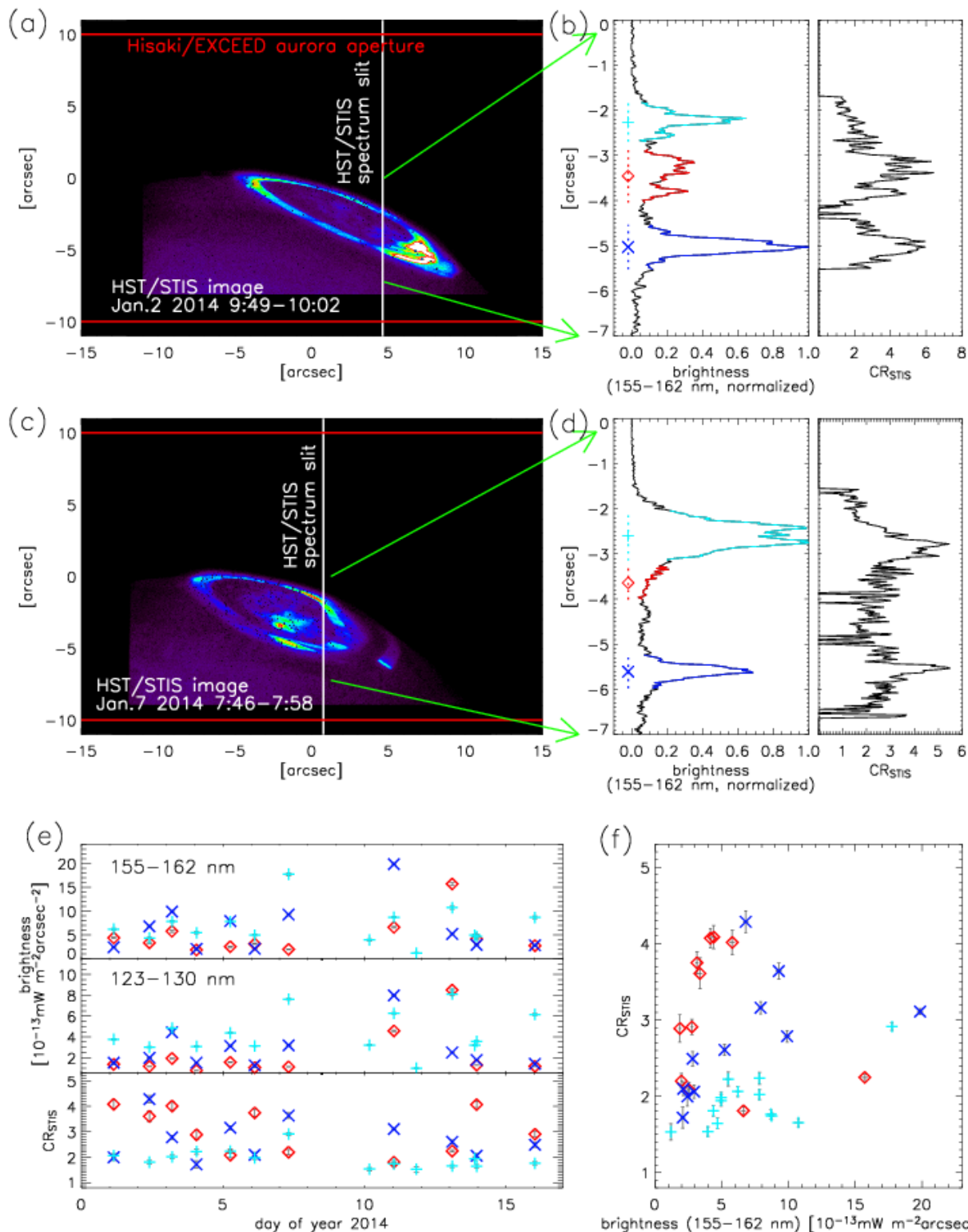
442

## 443 References

- 444 Badman, S. V., G. Branduardi-Raymont, M. Galand, S. Hess, N. Krupp, L. Lamy, H. Melin, and C.  
 445 Tao (2014), Auroral processes at the giant planets: Energy deposition, emission mechanisms,  
 446 morphology and spectra, *Space Sci. Rev.*, doi:10.1007/s11214-014-0042-x.
- 447 Bonfond, B., M. F. Vogt, J.-C. Gérard, D. Grodent, A. Radioti, and V. Coumans (2011), Quasi-periodic  
 448 polar flares at Jupiter: A signature of pulsed dayside reconnections?, *Geophys. Res. Lett.*, 38,  
 449 L02104, doi:10.1029/2010GL045981.
- 450 Clarke, J. T., D. Grodent, S. Cowley, E. Bunce, P. Zarka, J. Connerney, and T. Satoh (2004), Jupiter's  
 451 aurora, in *Jupiter: The Planet, Satellites and Magnetosphere*, edited by F. Bagenal, B. McKinnon,  
 452 and T. Dowling, pp. 639–670, Cambridge Univ. Press, Cambridge, U. K.
- 453 Clarke, J. T., et al. (2009), Response of Jupiter's and Saturn's auroral activity to the solar wind, *J.*  
 454 *Geophys. Res.*, 114, A05210, doi:10.1029/2008JA013694.
- 455 Connerney, J. E. P., M. H. Acuña, N. F. Ness, and T. Satoh (1998), New models of Jupiter's magnetic  
 456 field constrained by the Io flux tube footprint, *J. Geophys. Res.*, 103(A6), 11929–11939,  
 457 doi:10.1029/97JA03726.
- 458 Cowley, S. W. H., and E. J. Bunce (2001), Origin of the main auroral oval in Jupiter's coupled  
 459 magnetosphere-ionosphere system, *Planet. Space Sci.*, 49, 1067– 1088.

- 460 Cowley, S. W. H., J. D. Nichols, and D. J. Andrews (2007), Modulation of Jupiter's plasma flow, polar  
 461 currents, and auroral precipitation by solar wind-induced compressions and expansions of the  
 462 magnetosphere: A simple theoretical model, *Ann. Geophys.*, *25*, 1433–1463.
- 463 Gérard, J.-C., J. Gustin, D. Grodent, J. T. Clarke, and A. Grard (2003), Spectral observations of  
 464 transient features in the FUV Jovian polar aurora, *J. Geophys. Res.*, *108*(A8), 1319,  
 465 doi:10.1029/2003JA009901.
- 466 Gérard, J.-C., B. Bonfond, D. Grodent, A. Radioti, J. T. Clarke, G. R. Gladstone, J. H. Waite, D.  
 467 Bisikalo, and V. I. Shematovich (2014), Mapping the electron energy in Jupiter's aurora: Hubble  
 468 spectral observations, *J. Geophys. Res. Space Physics*, *119*, doi:10.1002/2014JA020514.
- 469 Grodent, D. (2014), A Brief Review of Ultraviolet Auroral Emissions on Giant Planets, *Space Sci Rev*,  
 470 doi: 10.1007/s11214-014-0052-8.
- 471 Grodent, D., J. H. Waite Jr., and J.-C. Gérard (2001), A self-consistent model of the Jovian auroral  
 472 thermal structure, *J. Geophys. Res.*, *106*(A7), 12,933–12,952.
- 473 Grodent, D., J.-C. Gérard, J. T. Clarke, G. R. Gladstone, and J. H. Waite Jr. (2004), A possible auroral  
 474 signature of a magnetotail reconnection process on Jupiter, *J. Geophys. Res.*, *109*, A05201,  
 475 doi:10.1029/2003JA010341.
- 476 Gustin, J., D. Grodent, J.-C. Gérard, and J. T. Clarke (2002), Spatially resolved far ultraviolet  
 477 spectroscopy of the Jovian aurora, *Icarus*, *157*, 91–103.
- 478 Gustin, J., J.-C. Gérard, D. Grodent, S. W. H. Cowley, J. T. Clarke, and A. Grard (2004), Energy-flux  
 479 relationship in the FUV Jovian aurora deduced from HST-STIS spectral observations, *J. Geophys.*  
 480 *Res.*, *109*, A10205, doi:10.1029/2003JA010365.
- 481 Gustin, J., et al. (2013), Effects of methane on giant planet's UV emissions and implications for the  
 482 auroral characteristics, *J. Mol. Spect.*, *291*, 108–117.
- 483 Harris, W., J. T. Clarke, M. A. McGrath, and G. E. Ballester (1996), Analysis of Jovian auroral H Ly-  
 484  $\alpha$  Emission (1981–1991), *Icarus*, *124*, 350–365.
- 485 Hill, T. W. (2001), The Jovian auroral oval, *J. Geophys. Res.*, *106*(A5), 8101–8107.
- 486 Kimura, T., et al. (2015), Transient internally driven aurora at Jupiter discovered by Hisaki and the  
 487 Hubble Space Telescope, *Geophys. Res. Lett.*, *42*, doi:10.1002/2015GL063272.
- 488 Livengood, T. A., and H. W. Moos (1990), Jupiter's north and south polar aurorae with IUE data,  
 489 *Geophys. Res. Lett.*, *17*(12), 2265–2268.
- 490 Livengood, T. A., T. Kostiuik, F. Espenak, and J. J. Goldstein (1993), Temperature and abundances in  
 491 the Jovian auroral stratosphere: 1. Ethane as a probe of the millibar region, *J. Geophys. Res.*,  
 492 *98*(E10), 18813–18822, doi:10.1029/93JE01043.
- 493 Nichols, J. D., J. T. Clarke, J. C. Gérard, D. Grodent, and K. C. Hansen (2009), Variation of different  
 494 components of Jupiter's auroral emission, *J. Geophys. Res.*, *114*, A06210,  
 495 doi:10.1029/2009JA014051.
- 496 Odstreil, D., and V. J. Pizzo (1999), Distortion of the interplanetary magnetic field by three-  
 497 dimensional propagation of coronal mass ejections in a structured solar wind, *J. Geophys. Res.*,  
 498 *104*(A12), 28225–28239, doi:10.1029/1999JA900319.
- 499 Pallier, L., and R. Prangé (2004), Detection of the southern counterpart of the Jovian northern polar  
 500 cusp: Shared properties, *Geophys. Res. Lett.*, *31*, L06701, doi:10.1029/2003GL018041.
- 501 Parkinson, C. D., J. C. McConnell, L. Ben Jaffel, A. Y. -T. Lee, Y. L. Yung, and E. Griffioen (2006),  
 502 Deuterium chemistry and airglow in the Jovian thermosphere, *Icarus*, *183*, 451–470.

- 503 Prangé, R., G. Chagnon, M. G. Kivelson, T.A. Livengood, and W. Kurth (2001), Temporal monitoring  
504 of Jupiter's auroral activity with IUE during the Galileo mission. Implications for magnetospheric  
505 processes, *Planet. Space Sci.*, *49*, 405–415.
- 506 Pryor, W. R. et al. (2005), Cassini UVIS observations of Jupiter's auroral variability, *Icarus*, *178*, 312–  
507 326.
- 508 Shiota, D., R. Kataoka, Y. Miyoshi, T. Hara, C. Tao, K. Masunaga, Y. Futaana, and N. Terada (2014),  
509 Inner heliosphere MHD modeling system applicable to space weather forecasting for the other  
510 planets, *Space Weather*, *12*, doi:10.1002/2013SW000989.
- 511 Tao, C., R. Kataoka, H. Fukunishi, Y. Takahashi, and T. Yokoyama (2005), Magnetic field variations  
512 in the Jovian magnetotail induced by solar wind dynamic pressure enhancements, *J. Geophys. Res.*,  
513 *110*, A11208, doi:10.1029/2004JA010959.
- 514 Tao, C., L. Lamy, and R. Prangé (2014), The brightness ratio of H Lyman- $\alpha$ /H<sub>2</sub> bands in FUV auroral  
515 emissions: A diagnosis for the energy of precipitating electrons and associated magnetospheric  
516 acceleration processes applied to Saturn, *Geophys. Res. Lett.*, *41*, doi:10.1002/2014GL061329.
- 517 Tao, C., T. Kimura, S. V. Badman, N. André, F. Tsuchiya, G. Murakami, K. Yoshioka, I. Yoshikawa,  
518 A. Yamazaki, and M. Fujimoto, Variation of Jupiter's Aurora observed by Hisaki/EXCEED: 2.  
519 Estimations of auroral parameters and magnetospheric dynamics, *J. Geophys. Res. Space Physics*,  
520 *120*, doi:10.1002/2015JA021272, accepted.
- 521 Vogt, M. F., M. G. Kivelson, K. K. Khurana, R. J. Walker, B. Bonfond, D. Grodent, and A. Radioti  
522 (2011), Improved mapping of Jupiter's auroral features to magnetospheric sources, *J. Geophys. Res.*,  
523 *116*, A03220, doi:10.1029/2010JA016148.
- 524 Waite J. H., Jr. et al. (2001), An auroral flare at Jupiter, *Nature*, *410*, 787–789, doi:10.1038/35071018.
- 525 Yamazaki, A. et al. (2014), Field-of-view guiding camera on the HISAKI (SPRINT-A) satellite, *Space*  
526 *Sci. Rev.*, *184*, 1–4, 259–274, DOI: 10.1007/s11214-014-0106-y.
- 527 Yoshikawa, I. et al. (2014), Extreme ultraviolet radiation measurement for planetary  
528 atmospheres/magnetospheres from the earth-orbiting spacecraft (Extreme Ultraviolet Spectroscope  
529 for Exospheric Dynamics: EXCEED), *Space Sci. Rev.*, *184*, 1–4, 237–258, DOI:10.1007/s11214-  
530 014-0077-z.
- 531 Yoshioka, K. et al. (2013), The extreme ultraviolet spectroscope for planetary science, EXCEED,  
532 *Planet. Space Sci.*, *85*, 250–260.
- 533 Yung, Y. L., G. R. Gladstone, K. M. Chang, J. M. Ajello, and S. K. Srivastava (1982), H<sub>2</sub> fluorescence  
534 spectrum from 1200 to 1700 Å by electron impact: laboratory study and application to Jovian aurora,  
535 *Astrophys. J.*, *254*, L65-69.
- 536

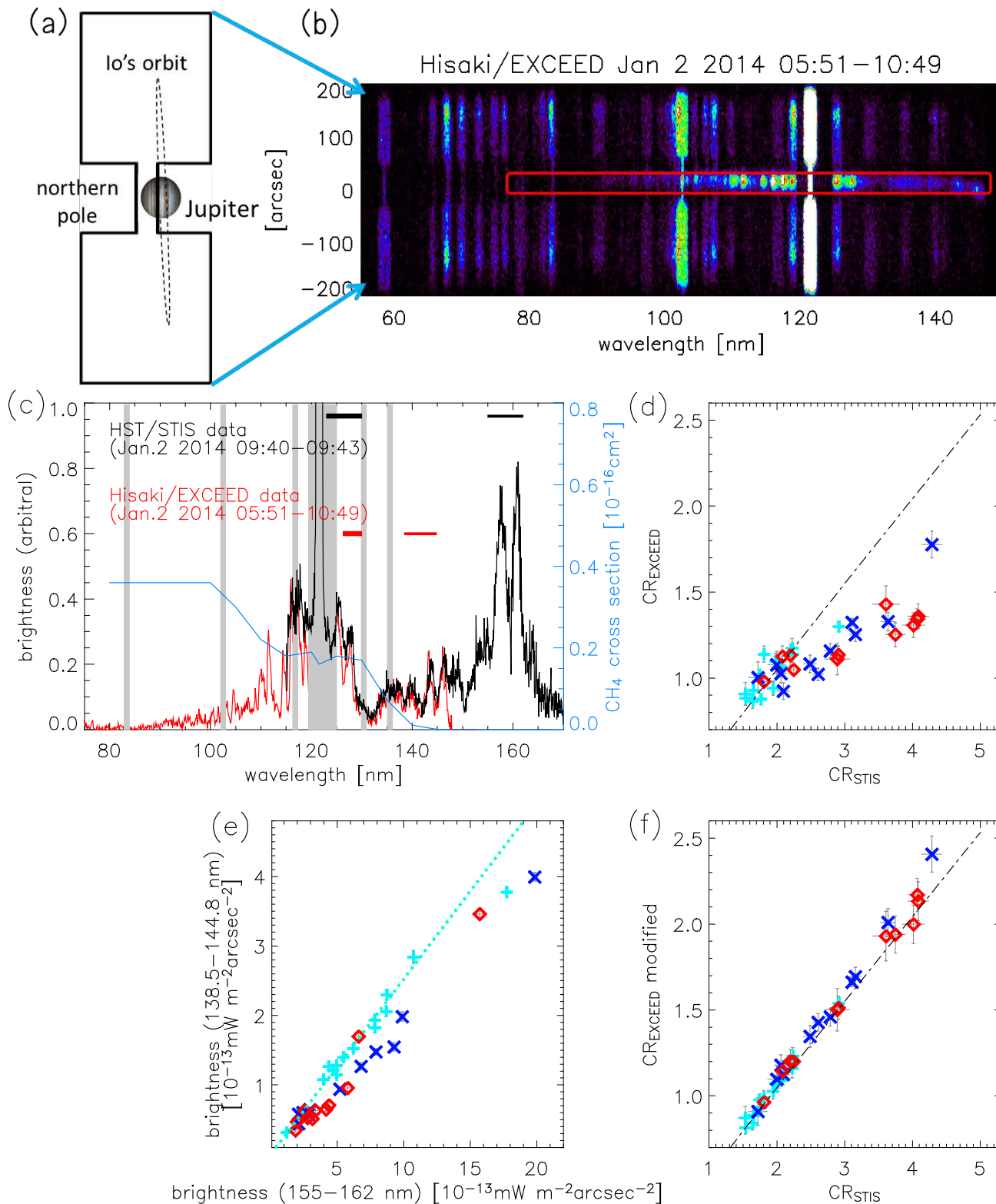


537

538 Figure 1. (a) Image of Jupiter’s northern polar region, (b) the spatial profiles of the observed brightness  
 539 integrated over wavelengths of 155–162 nm (left) and the CR (right) from the spectral observation  
 540 along the slit on 2 January 2014, (c) the image and (d) the spatial profiles of the brightness and CR  
 541 observed on 7 January 2014, (e) the time variations of the auroral brightness emitted at wavelengths  
 542 (top) of 155–162 nm and (middle) of 123–130 nm, and (bottom) the time variation of the CR, and (f)  
 543 the relationship between the brightness at wavelengths 155–162 nm and the colour ratio. The values  
 544 in Figures 1e and 1f are taken at the main auroral oval on the disk (blue crosses), main auroral oval at

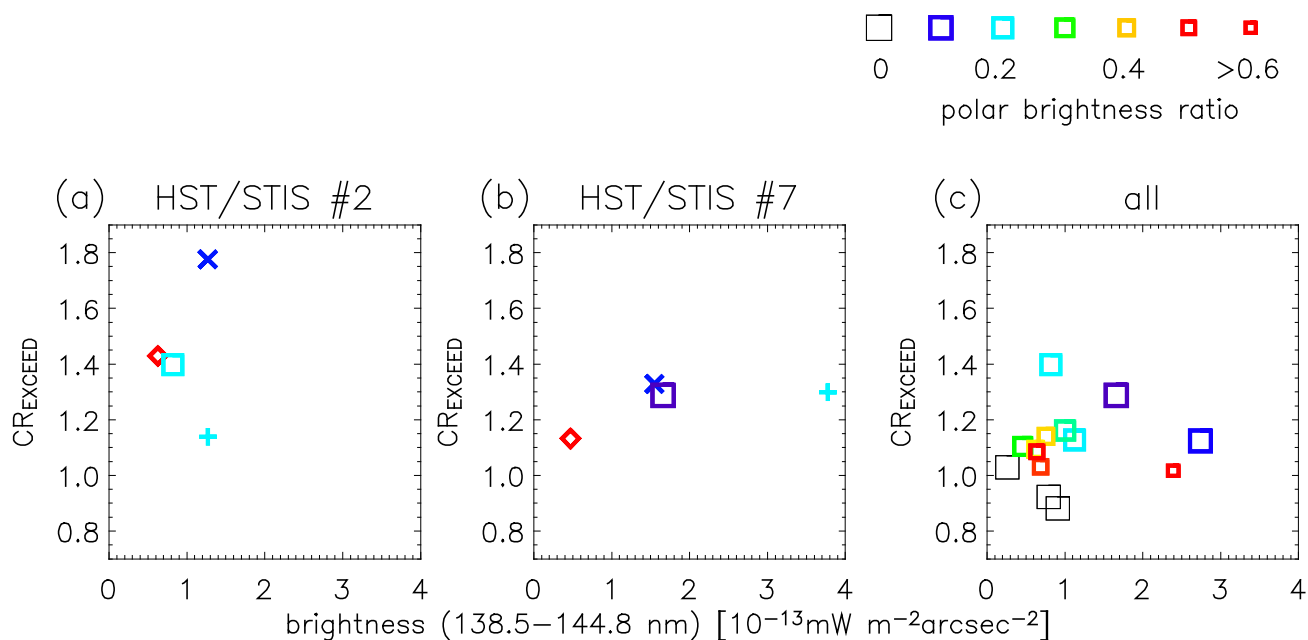
545 the limb (light blue pluses), and high-latitude polar region (red diamonds) along the spectral slit, with  
 546 error bars (grey lines). The corresponding auroral structures are shown using the same colours in the  
 547 left panel of Figures 1b and 1d for 2 and 7 January, respectively. Figures 1a and 1c are shown in the  
 548 same linear colour scale. The aurora aperture of EXCEED is bounded by the two red lines in Figures  
 549 1a and 1c, and white vertical lines show the positions of the STIS slit for the spectral observations.  
 550

551



552  
553

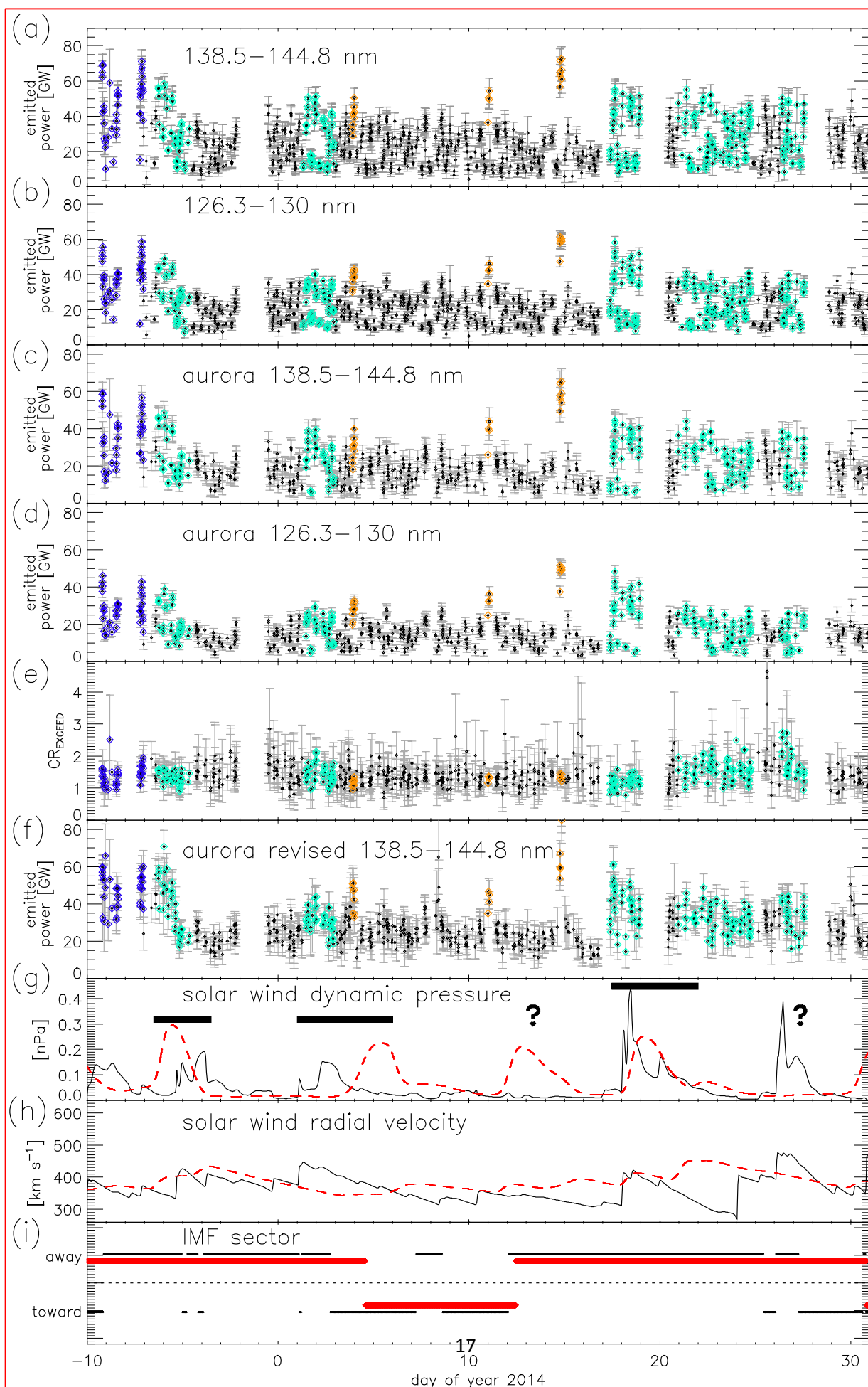
554 Figure 2. (a) Schematics of the observation geometry of EXCEED using the dumbbell-shaped slit, (b)  
 555 imaging spectrum measured by EXCEED, (c) auroral spectra measured on 2 January by STIS  
 556 integrated over the slit (black) and by EXCEED over the full polar region (red), and the relationships  
 557 (d) between the two colour ratios,  $CR_{STIS}$  and  $CR_{EXCEED}$ , determined from the STIS spectra (e) between  
 558 the brightness at the wavelength bands less affected by absorption selected for the STIS (155–162 nm)  
 559 and EXCEED (138.5–144.8 nm), and (f) between  $CR_{STIS}$  and modified  $CR_{EXCEED}$ , estimated using  
 560 STIS spectra. The values for the main auroral oval (blue crosses), main auroral oval at the limb (light-  
 561 blue pluses), and high-latitude region (red diamonds) with error bars (grey lines) were derived. In  
 562 Figure 2c, the grey hatched regions correspond to the H Lyman, He, and O emission lines from  
 563 geocorona. The absorption cross section for methane [Parkinson et al., 2006] is indicated by the blue  
 564 line corresponding to the right-hand axis, and the two wavelength bands used for the CR estimations  
 565 are shown using the horizontal lines. The dot-dashed line in Figures 2d and 2f shows the reference  
 566 relation between  $CR_{STIS}$  and  $CR_{EXCEED}$  based on the  $CH_4$  absorption effect. The light blue dotted line  
 567 in Figure 2e is the best fit to the brightness values obtained for the main aurora at the limb.  
 568  
 569



570  
 571

572 Figure 3. Relationships between the auroral emitted power at wavelengths of 155–162 nm and the CR  
 573 using the similar format as Figure 1f for observations (a) on 2 January 2014 and (b) on 7 January 2014.  
 574 The squares indicate the values estimated from the observation integrated over the entire auroral region  
 575 along the slit in each observation, and those for all events are shown in Figure 3c. The colour and size  
 576 of the squares represent the ratio of the brightness of the high-latitude region to the total auroral  
 577 brightness integrated along the slit according to the legend at the top.  
 578

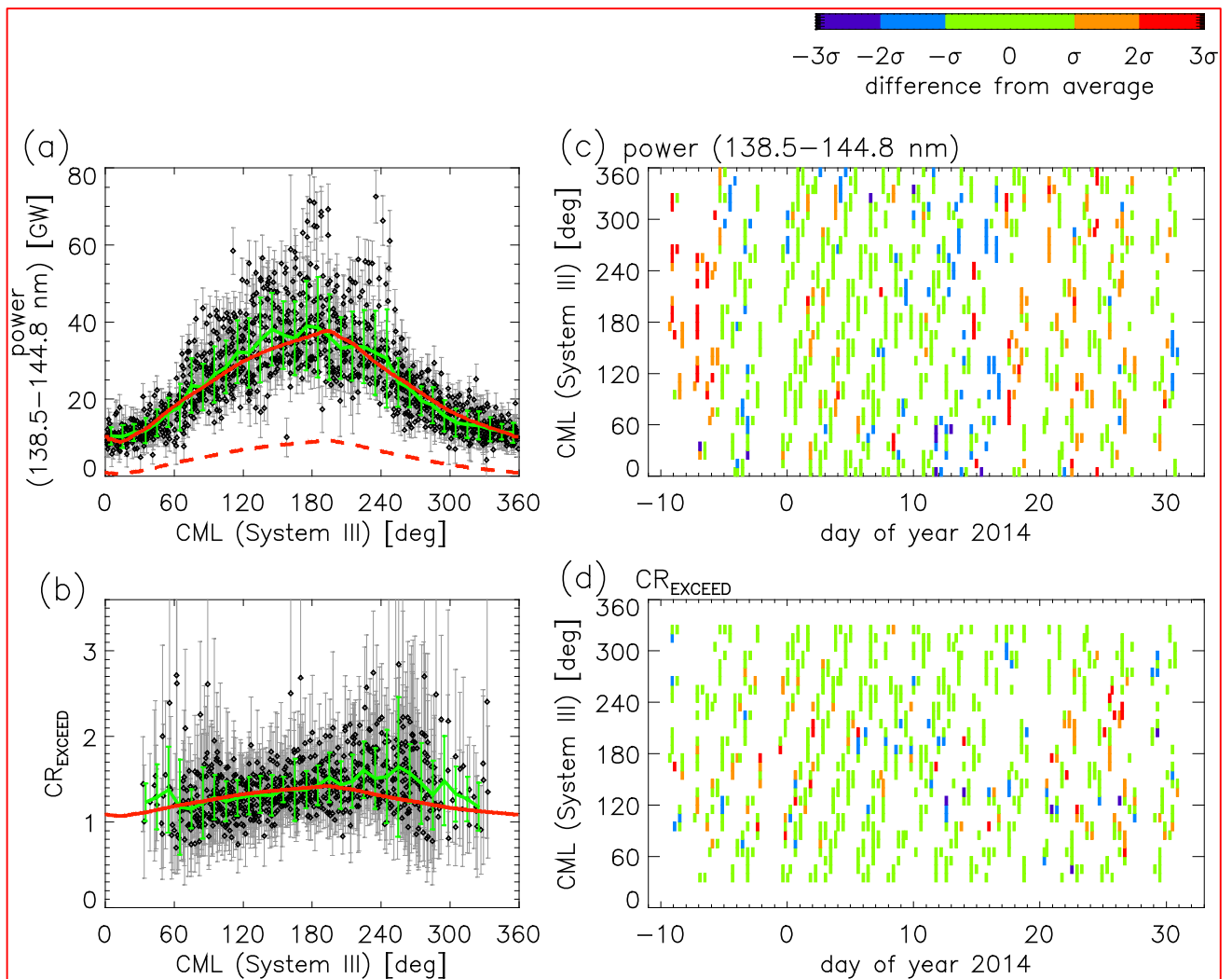




580

581 Figure 4. Time variations of the total power emitted at wavelengths (a) of 138.5–144.8 nm and (b)  
 582 126.3–130 nm, and (c–d) those from aurora (with background subtraction, see the text), (e) CR,  
 583 observed with EXCEED (black points) with error bars representing photon statistics errors (grey lines),  
 584 (f) the emitted power scaled for visibility of the auroral region, and time variations of the solar wind  
 585 (g) dynamic pressure, (h) radial velocity, and (i) the IMF sector, estimated using a 1D model (black lines)  
 586 and SUSANOO (thick or dashed red lines). The periods of short-term and long-term auroral  
 587 emitted power enhancements are shown using the horizontal orange short and light blue long bars in  
 588 Figure 4a, respectively, except for the intermittent observation before DOY-7 as shown using the blue  
 589 ticks. The solar wind dynamic pressure enhancements observed in both the 1D and SUSANOO models  
 590 are shown using the horizontal thick bars in Figure 4g.

591

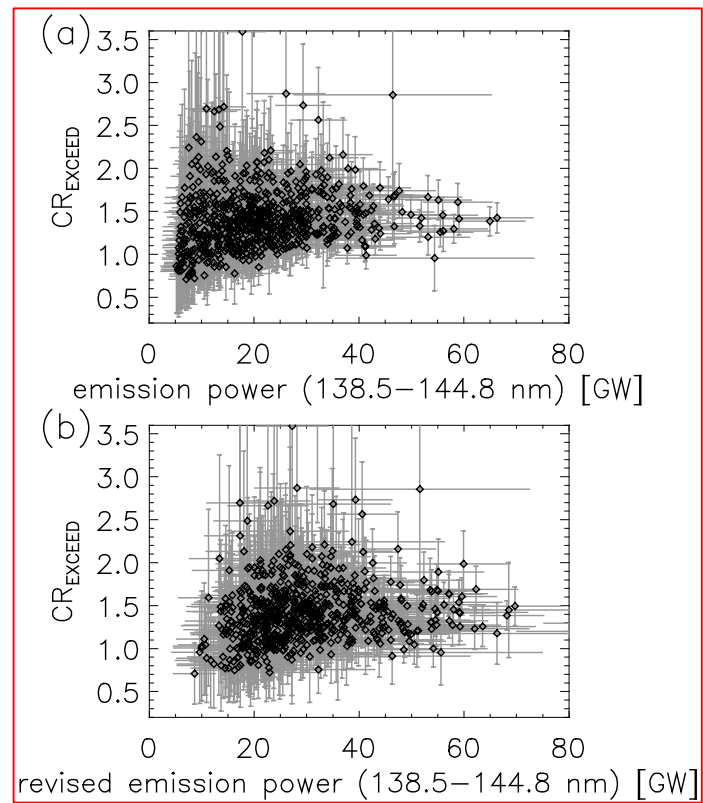


592

593 Figure 5. (a) Power emitted at wavelengths of 138.5–144.8 nm and (b) CR<sub>EXCEED</sub> shown as a function  
 594 of the System III CML over DOYs from -11 to 31 2014, and the colour maps of (c) the power emitted  
 595 at wavelengths of 138.5–144.8 nm and (d) CR<sub>EXCEED</sub> normalized by standard deviations  $\sigma$  in 36 CML  
 596 bins (as in colour bars), as functions of the time and the CML. In Figures 5a and 5b, the black dots are  
 597 observed points and the grey lines show their errors, and the average values in 36 CML bins are shown  
 598 using the green lines with error bars representing the standard deviation. The red solid lines in Figures  
 599 5a and 5b are the fits to the average of each parameter using the relative northern auroral area shown  
 600 by the red dashed line in Figure 5a.

601

602



603

604

605 Figure 6. (a) Relationship between the power emitted at wavelengths of 138.5–144.8 nm and  $CR_{EXCEED}$ ,  
606 and (b) relationship between the scaled emitted power (scaled for visibility of the auroral region) and  
607  $CR_{EXCEED}$ . The observed relations are shown using the black points.

608

609

610

611

612 Table 1. Summary of the imaging and spectral observations conducted using the STIS: date, start time  
 613 in UT, corresponding CML, brightness over 155–162 nm,  $CR_{STIS}$ , brightness over 138.5–144.8 nm,  
 614 and  $CR_{EXCEED}$  derived from the STIS spectra at the main aurora on the disk, emitted power over 138.5–  
 615 144.8 nm, and  $CR_{EXCEED}$  derived from the EXCEED observation at the timing closest to the STIS  
 616 spectral observation of each event.

#	Date 2014	STIS image observation 1 (exposure 700 sec.)		STIS spectral observation (exposure 200 sec.)		STIS image observation 2 (exposure 736 sec.)		STIS spectra values of the main aurora on the disk				EXCEED values closest to the STIS spectral observation	
		Start time (UT)	CML [°]	Start time (UT)	CML [°]	Start time (UT)	CML [°]	Bright ness (155– 162 nm) <sup>a</sup>	CR <sub>STIS</sub>	Brightn ess (138.5– 144.8 nm) <sup>a</sup>	CR <sub>E</sub> <sub>XCEE</sub> <sub>D</sub>	Emitted Power (138.5– 144.8 nm) [GW] <sup>c</sup>	CR <sub>E</sub> <sub>XCEE</sub> <sub>D</sub>
1	Jan 1	03:02	173	03:23	186	03:32	191	2.4	2.0	0.60	1.1	24.	1.1
2	Jan 2	09:19	192	09:40	204	09:49	210	6.8	4.3	1.3	1.8	27.	1.6
3	Jan 3	04:27	166	04:47	178	04:57	184	9.9	2.8	2.0	1.2	19.	1.4
4	Jan 4	01:10	197	01:31	210	01:40	215	2.1	1.7	0.58	1.0	32.	1.2
5	Jan 5	05:52	158	06:12	171	06:21	176	7.9	3.2	1.5	1.3	26.	1.4
6	Jan 6	02:35	190	02:55	202	03:05	208	2.1	2.1	0.44	0.92	18.	1.1
7	Jan 7	07:16	151	07:37	163	07:46	169	9.3	3.6	1.5	1.3	24.	1.6
8	Jan 10	03:48	117	04:09	129	04:18	135	-- <sup>b</sup>	-- <sup>b</sup>	-- <sup>b</sup>	-- <sup>b</sup>	22.	1.4
9	Jan 11	00:31	149	00:52	161	01:01	167	19.9	3.1	4.0	1.3	40.	1.4
10	Jan 11	19:39	122	20:00	134	20:09	140	-- <sup>b</sup>	-- <sup>b</sup>	-- <sup>b</sup>	-- <sup>b</sup>	22.	1.2
11	Jan 13	01:56	141	02:16	153	02:26	159	5.2	2.6	0.94	1.0	22.	1.5
12	Jan 13	21:03	115	21:24	127	21:33	133	-- <sup>b</sup>	-- <sup>b</sup>	-- <sup>b</sup>	-- <sup>b</sup>	19.	1.4
13	Jan 13	22:39	172	22:59	185	23:09	191	2.9	2.1	0.62	1.1	17.	1.3
14	Jan 16	00:03	165	00:24	177	00:33	183	2.8	2.5	0.57	1.1	11.	1.1

617 a) unit is  $10^{-13}$  mW m<sup>-2</sup> arcsec<sup>-2</sup>.

618 b) the STIS slit only crosses the aurora at the limb

619 c) the auroral power after the background subtraction, without scaling for visibility of the auroral  
 620 region

621